RSC Advances

ROYAL SOCIETY OF CHEMISTRY

www.rsc.org/advances

Synthesis of Eu^{3+}-activated BiOF and BiOBr phosphors: Photoluminescence, Judd-Ofelt analysis and photocatalytic properties

Rohit Saraf[a], C. Shivakumara[a,*], Sukanti Behera[a], N. Dhananjaya[b] and H. Nagabhushana[c]

[a]*Solid State and Structural Chemistry Unit, Indian Institute of Science, Bangalore 560012, India.*

[b]*Department of Physics, B.M.S. Institute of Technology, Bangalore 560 064, India.*

[c]*C. N. R. Rao Center for Advanced Materials, Tumkur University, Tumkur 572 103, India.*

*** Corresponding Author**

C. Shivakumara. E-mail: shiva@sscu.iisc.ernet.in

Telephone : +91 80 2293 2951; FAX : +91 80 2360 1310

Abstract

Series of $Bi_{1-x}Eu_xOX$ (X = F and Br; x = 0, 0.01, 0.03 and 0.05) phosphors were synthesized at relatively low temperature and shorter duration (500 °C, 1 h). Rietveld refinement results verified that all the compounds were crystallized in the tetragonal structure with space group *P4 /nmm* (No. 129). Photoluminescence spectra exhibit characteristic luminescence $^5D_0 \rightarrow {}^7F_J$ (J = 0–4) intra-4f shell Eu^{3+} ion transitions. The magnetic dipole ($^5D_0 \rightarrow {}^7F_1$) transition dominates the emission of BiOF: Eu^{3+}, while the electric dipole ($^5D_0 \rightarrow {}^7F_2$) peak was stronger in BiOBr: Eu^{3+} phosphors. The evaluated CIE color coordinates for $Bi_{0.95}Eu_{0.05}OBr$ (0.632, 0.358) is close to the commercial Y_2O_3:Eu^{3+} (0.645, 0.347) and Y_2O_2S: Eu^{3+} (0.647, 0.343) red phosphors. Intensity parameters (Ω_2, Ω_4) and various radiative properties such as transition rates (A), branching ratios (β), stimulated emission cross-section (σ_e), gain bandwidth ($\sigma_e \times \Delta\lambda_{eff}$) and optical gain ($\sigma_e \times \tau$) were calculated using the Judd-Ofelt theory. It was observed that BiOBr: Eu^{3+} phosphors have a long lifetime (τ) and better optical gain ($\sigma_e \times \tau$) as compared to reported Eu^{3+} doped materials. Further, these compounds exhibit excellent photocatalytic activity for the degradation of rhodamine B dye under visible light irradiation. The determined radiative properties and photocatalytic results revealed that BiOBr: Eu^{3+} phosphors have the potential applications in energy and environmental remedies, such as to develop red phosphors for white light-emitting diodes, red lasers and to remove toxic organic industrial effluents .

Keywords: BiOF; BiOBr; Phosphors; Judd-Ofelt analysis; Photocatalytic activity.

1. Introduction

Rare earth activated phosphor materials have been attracting much attention based on their applications in various fields, such as plasma display panels, mercury free lamps, white light-emitting diodes (WLEDs) and cathode ray tubes.[1–3] Among them, WLEDs have been considered as one of the most promising technologies in the solid state lighting industry due to their high efficiency, compactness, long operational lifetime, better color quality, low energy consumption and lack of toxic mercury.[4] WLEDs have high promise to replace traditional incandescent and fluorescent lamps as a next generation general lighting.[5] Rare-earth activated phosphor materials for LEDs have gained interest due to their characteristic sharp transitions arising from inner 4f orbitals.[6] Especially, the red emitting trivalent Eu^{3+}-activated phosphors have significant importance because of their potential application in color display and lighting technologies. This was because the lowest excited level ($^5D_0$) of the $4f^6$ configuration in Eu^{3+} was situated below the $4f^5$5d configuration. Trivalent europium ions exhibited narrow band emissions, long lifetimes and large Stokes shifts (emission of lower energy radiation upon excitation by higher energy radiation).[7]

Various inorganic phosphors have been reported, including molybdates,[7] silicates,[8] phosphates,[9] tungstates,[10] aluminates,[11] nitrides[12] and sulfides[13]. These materials are either chemically unstable, expensive or have low fluorescent lifetime. Therefore, in order to improve the performances of red phosphors in white LEDs, it is urgent to seek alternative red phosphors with long lifetime, high chemical stability and better quality. Bismuth oxyhalides are interesting luminescent materials due to their unique layered structures and high chemical stability.[6] The efficient energy transfer from the host matrix to the localized states of lanthanide ions also benefits the luminescence property. Moreover, bismuth oxyhalides have been found to exhibit

various applications in photocatalysis, pharmaceuticals, battery cathodes and photoelectrochemical devices.[14,15]

Bismuth oxyhalides have been widely used in photocatalytic applications due to their strong intralayer bonding and weak interlayer van der Waals interaction. The layered structure can provide the space large enough to polarize the related atoms and orbitals. The induced dipole between these layers assists in the effective separation of photogenerated electron–hole pairs. Many studies have been reported on the degradation of organic dyes under UV and visible light irradiation.[16–25] However, bismuth oxyhalides with good photocatalytic efficiency under visible light irradiation are less reported. Further, several methods have been employed for the synthesis of bismuth oxyhalides, namely microwave irradiation,[6] sol-gel,[17] hydrolysis,[18] hydrothermal,[20] solvothermal,[22] solution oxidation[24] and sonochemical[25] methods. All these synthesis methods involve several problems, such as high pressure, less yield, lack of composition control, requirement of solvents, long reaction time and capping agent. The solid state method offer several advantages over other conventional methods such as mass scale production, higher purity of products, better compositional control and solvent/surfactant free process.

To our knowledge, the spectroscopic properties of Eu^{3+}-activated bismuth oxyfluoride and oxybromide are rarely reported. Therefore, in this paper, we report series of Eu^{3+}-activated BiOF and BiOBr phosphors which can meet the requirements of red phosphors in WLEDs as well as useful in environmental sustainability applications. The crystallographic structural parameters, functional groups and morphology were analyzed by powder X-ray diffraction (XRD), Fourier transform infrared (FTIR) spectroscopy and Scanning electron microscopy (SEM), respectively. UV-Visible and photoluminescence (PL) properties were investigated. Judd–Ofelt theory was applied to calculate the intensity parameters and various other radiative

properties such as radiative transition rates, branching and asymmetry ratios, stimulated emission cross-section, gain bandwidth and optical gain. In addition, these compounds were used as photocatalysts for the degradation of rhodamine B (RhB) dye under visible light irradiation.

2. Experimental Section

2.1. Synthesis

$Bi_{1-x}Eu_xOX$ (X = F and Br; x = 0, 0.01, 0.03 and 0.05) compounds were synthesized by the conventional solid state method. For the synthesis of host BiOF, Bi_2O_3 (1.1649 g) and NH_4F (0.2223 g, 20% excess) were used as the raw materials and were ground finely in an agate mortar with pestle. This mixed powder was transferred into porcelain crucible and calcined at 400 °C for 1 h (ambient atmosphere) and cooled down to room temperature. Further, Eu^{3+}-activated BiOF compounds were prepared by taking an appropriate amount of Eu_2O_3 as the starting material. Similarly, the series of $Bi_{1-x}Eu_xOBr$ compounds were synthesized by choosing NH_4Br in place of NH_4F as a starting material and calcined at 500 °C for 1 h. The equation for the formation of $Bi_{1-x}Eu_xOX$ compounds is represented by the following reaction:

$$(1\text{-}x)\ Bi_2O_3 + x\ Eu_2O_3 + 2\ NH_4X \rightarrow 2\ Bi_{1-x}Eu_xOX + 2\ NH_3 + H_2O \quad (1)$$

2.2. Characterization

Powder X-ray diffraction patterns were measured by using PANalytical X'Pert Pro Powder diffractometer with Cu Kα radiation (λ = 1.5418 Å) source and a nickel filter. Rietveld refinement data were collected at a scan rate of 1˚/ min with a 0.02˚ step size for 2θ from 10˚ to 80˚. Structural parameters were estimated by Rietveld refinement method using FullProf Suite-2000 program. Surface morphology and composition analysis of these compounds were

investigated using SEM (FEI Quanta 200). FTIR spectra were recorded using Perkin Elmer Spectrometer, Frontier using KBr as a reference. UV–Visible absorption spectra have been recorded for powders on Perkin Elmer Lambda 750 spectrophotometer. TGA analysis was performed using Mettler-Toledo system in the presence of N_2 as a carrier gas upto 900 °C. Photoluminescence studies have been carried out using a JobinYvon spectrofluorometer (Fluorolog-3, Horiba) equipped with a 450 W xenon lamp as the excitation source. The photoluminescence (PL) decay lifetime measurements were performed at low temperature (77 K) with a Perkin Elmer spectrofluorimeter. The photocatalytic activity of rhodamine B dye solution was analyzed by Perkin Elmer UV–Visible spectrophotometer (Lambda 35) in the range from 200 to 800 nm periodically. All the measurements were performed at room temperature.

2.3. Measurement of photocatalytic activity

The photocatalytic activities of $Bi_{1-x}Eu_xOX$ compounds were measured by examining the degradation of RhB dye under visible-light irradiation ($\lambda \geq 420$ nm). A 500 W metal halide lamp held at 15 cm from the sample was used as the visible-light source. In each experiment, 50 mg of photocatalysts was added into 50 ml of RhB solution with a concentration of 1×10^{-5} M. Prior to Visible illumination, the suspensions were magnetically stirred in the dark for 30 min to ensure an adsorption-desorption equilibrium. Then, the stable aqueous dye solution was exposed to visible light. During the photoreaction, about 3 ml of suspension was collected at different time intervals and centrifuged to remove the catalyst. The transparent solution was analyzed using a UV–Vis spectrophotometer, and the absorbance was measured at a wavelength of 554 nm, which corresponds to the maximum absorption wavelength of RhB. The degradation efficiency of RhB was calculated using the following expression,

$$\text{RhB degradation } (\%) = \frac{C_0 - C}{C_0} \times 100 \quad (2)$$

where C_0 is the initial concentration at 0 min and C is the concentration at time t.

3. Results and discussion

3.1. Powder X-ray diffraction

Phase purity of $Bi_{1-x}Eu_xOX$ compounds were identified by powder X-ray diffraction. Fig. 1(a) and (b) shows the indexed XRD patterns of $Bi_{1-x}Eu_xOF$ and $Bi_{1-x}Eu_xOBr$ compounds, respectively. The strong diffraction peaks revealed the crystalline nature of the samples. The observed diffraction peaks of Eu^{3+} activated BiOF and BiOBr compounds match well with the reported JCPDS Card No. 86–1648 and 85–0862, respectively. No traces of additional peaks were observed in the XRD patterns, which confirmed that the Eu^{3+} ions have been uniformly incorporated into the host lattice of BiOX. This implies that the powders obtained by solid state reaction were single phase materials. The structural parameters were refined by the Rietveld method using powder XRD data. The patterns were typically refined for lattice parameters, scale factor, backgrounds, pseudo-Voigt profile function (u, v and w), atomic coordinates and isothermal temperature factors (B_{iso}). The refinement results confirmed that all the compounds were crystallized in the tetragonal phase with space group *P4/nmm* (No. 129). The observed, calculated and the difference XRD patterns of $Bi_{1-x}Eu_xOX$ compounds are shown in Fig. 2. The difference between XRD pattern profiles experimentally observed and calculated data display near to zero in the intensity scale as illustrated by a line (Y_{obs} - Y_{calc}). The refined structural parameters for $Bi_{1-x}Eu_xOX$ (X = F and Br) compounds are summarized in Table 1 and Table 2. It was observed that the lattice parameters and cell volumes increase with increasing ionic radii of

X (X = F (r_{F^-} = 1.33 Å) and Br (r_{Br^-} = 1.96 Å)) in BiOX. Further, there was no appreciable change in these parameters upto 5 mol% substitution of Eu^{3+} ion in both compounds. This was due to the substitution of smaller Eu^{3+} ion ($r_{Eu}{}^{3+}$ = 1.066 Å) to larger Bi^{3+} ion ($r_{Bi}{}^{3+}$ = 1.17 Å).

The crystal structure of BiOF was modeled using Rietveld refined structural parameters by VESTA program (Fig. S1). In the BiOF structure, the Bi^{3+} atom was coordinated to a square antiprism with four O atoms in one base and four F atoms in another base. The BiOF layers were stacked over one another by the nonbonding van der Waals interaction through fluoride atoms along the c-axis. The crystal structure of the BiOF and BiOBr matrices were same, but the interplanar lattice spacings were different. The distance between two bismuth ions in adjacent BiOX (X = F and Br) layers was found to be 3.63 and 5.57 Å for BiOF and BiOBr crystals, respectively.

3.2. SEM analysis

Fig. 3 shows the surface morphology of $Bi_{1-x}Eu_xOX$ compounds obtained by solid state method. For BiOF and $Bi_{0.95}Eu_{0.05}OF$ compounds, the micrographs revealed agglomerated granules with an average diameter in the range of 0.349 to 0.689 μm (Fig. 3(a) and (b)). Fig. 3(c) and (d) shows SEM images of BiOBr and $Bi_{0.95}Eu_{0.05}OBr$ compounds, respectively. The micrographs show the plate-like morphology with an average thickness of 0.185–0.272 μm. To confirm the homogeneity of elements in the compounds, we have carried out the elemental mapping using energy dispersive X-ray (EDX) analysis. Figs. S2 and S3 show the elemental mapping of BiOF and $Bi_{0.95}Eu_{0.05}OF$ compounds, respectively. The elemental mapping of BiOF confirmed that all the elements were homogeneously distributed over the entire area. For 5 mol%

Eu^{3+} doping, although the concentration of Eu was low and therefore faintly visible but was evenly distributed.

3.3. FTIR studies

The purity and functional groups of $Bi_{1-x}Eu_xOX$ compounds were confirmed by the FTIR spectra. The spectra were measured in the wave number region of 500–1500 cm^{-1} (Fig. 4). In $Bi_{1-x}Eu_xOF$ compounds, the vibration peak of metal-oxygen bond (Bi–O) appeared at about 563 cm^{-1}. For $Bi_{1-x}Eu_xOBr$ compounds, the symmetrical stretching vibration originating from the Bi–O was located around 510 cm^{-1}. It was observed that the peak shifted towards lower frequency with increasing atomic number and ionic radii of X. This was due to the heavier atoms which cause the attached bonds absorb at lower frequencies.

3.4. UV-Vis absorption spectroscopy

The optical property of $Bi_{1-x}Eu_xOX$ compounds was studied by UV–Vis diffuse reflectance spectroscopy (Fig. 5). The intense absorption edge of BiOF and BiOBr compounds were found to be around 445 and 495 nm, respectively. It was observed from the UV-Vis absorption spectra that there was a red shift in the absorption edges of BiOX powders with increasing atomic number of X. The optical energy band gap (E_g) of $Bi_{1-x}Eu_xOX$ compounds were estimated from UV-Vis absorption spectra using Wood and Tauc relation.[26] The energy band gap was calculated with absorbance and photon energy by the following equation:

$$\alpha h\nu = A\left(h\nu - E_g\right)^n \quad (3)$$

where α is the absorption coefficient, $h\nu$ is the photon energy, A is a proportional constant, E_g is the energy band gap and n depends on the characteristics of the transition in a semiconductor. (n = 1/2, 2, 3/2, or 3 for allowed direct, allowed indirect, forbidden direct, and forbidden indirect

electronic transitions, respectively). BiOF exhibits a direct band gap (n = 1/2), while BiOBr presents an indirect band gap (n = 2).[27] The intercept of the tangent to the x-axis gives good approximation of the band gap energies of $Bi_{1-x}Eu_xOF$ and $Bi_{1-x}Eu_xOBr$ compounds from 2.79–2.86 and 2.5–2.59 eV, respectively (Fig. 5(a) and (b)). These values revealed that the calculated band gap energy decreases with increasing atomic number of X, which is consistent with the experimentally observed trend. The obtained band gap energy values of BiOF and BiOBr were close to the reported values in the literature.[27] On substitution of smaller Eu^{3+} ion (r_{Eu}^{3+} = 1.066 Å) to larger Bi^{3+} ion (r_{Bi}^{3+} = 1.17 Å), the band gap value increases in $Bi_{1-x}Eu_xOX$ compounds.

3.5. Thermogravimetric analysis

Thermogravimetric analysis (TGA) was used to evaluate the thermal stability of BiOF and BiOBr compounds. The total weight loss of BiOF in the heat treatment from room temperature to 900 °C was determined to be 7% in Fig. S4. While in BiOBr compound, 30% weight loss was observed in the range of 560 to 695 °C due to the decomposition of BiOBr into bismuth oxide and bromine. Further, the decomposition of bismuth oxide was started above 695 °C. This fact indicates that the thermal stability of BiOX decreases with increasing X atomic number, which was due to the co-contribution of the lattice parameters and interatomic binding energies.[28]

3.6. Photoluminescence properties

Fig. 6 shows the excitation (a) and emission (b) spectra of $Bi_{1-x}Eu_xOF$ phosphors. The excitation spectrum monitored at 592 nm consists of three sharp peaks between 320 and 500 nm. The sharp peaks located at 378 nm ($^7F_0 \rightarrow {}^5G_2$), 395 nm ($^7F_0 \rightarrow {}^5L_6$) and 465 nm ($^7F_0 \rightarrow {}^5D_2$) were the characteristic 4f–4f transitions of Eu^{3+} ions in the host lattice. Upon excitation at 395 nm, the emission spectra exhibit a group of similar emission lines, which correspond to

transitions from the excited $^5D_0$ level to the ground ^7F_J (J = 0, 1, 2, 3, and 4) levels of the Eu^{3+} $4f^6$ configuration. The sharp peaks in the emission spectra were correspond to the electronic transitions as $^5D_0 \rightarrow {}^7F_0$ (579 nm), $^5D_0 \rightarrow {}^7F_1$ (592 nm), $^5D_0 \rightarrow {}^7F_2$ (617 nm), $^5D_0 \rightarrow {}^7F_3$ (648 nm) and $^5D_0 \rightarrow {}^7F_4$ (698 nm). Fig. S5 depicts the energy level diagram for Eu^{3+}-activated BiOF phosphors. The presence of unique emission line at 579 nm was due to the J–J mixing by the crystal field effects. The $^5D_0 \rightarrow {}^7F_1$ transition peak originates from magnetic dipole transition. In contrast, the radiative transitions from $^5D_0$ to $^7F_2$ and $^7F_4$ levels were electric dipole in character.[7, 10] The $^5D_0 \rightarrow {}^7F_3$ transition was forbidden from both electric and magnetic dipole considerations. The $^5D_0 \rightarrow {}^7F_J$ emission of the Eu^{3+} ion has a close relationship with its occupied chemical environment. When the Eu^{3+} ion was located at site with inversion symmetry, the magnetic dipole ($^5D_0 \rightarrow {}^7F_1$) emission transition was dominant, whereas at site without inversion symmetry, the electric dipole ($^5D_0 \rightarrow {}^7F_2$) transition becomes dominant.[10] For $Bi_{1-x}Eu_xOF$ phosphors, the emission intensity of $^5D_0 \rightarrow {}^7F_1$ was stronger than that of $^5D_0 \rightarrow {}^7F_2$, which indicates that the Eu^{3+} ion mainly occupies the site with inversion symmetry in the BiOF host lattice. In addition, the intensity of the emission peaks increase with the increase in Eu^{3+} doping concentration from 1 to 5 mol%.

Fig. 7(a) exhibits the PL excitation spectrum of $Bi_{0.99}Eu_{0.01}OBr$ phosphor when monitored at λ_{em} = 614 nm. The excitation peaks at 382 nm, 395 nm and 411 nm were observed which correspond to $^7F_0 \rightarrow {}^5G_2$, $^7F_0 \rightarrow {}^5L_6$ and $^7F_0 \rightarrow {}^5D_3$ transitions of Eu^{3+}, respectively. The emission spectra obtained for $Bi_{1-x}Eu_xOBr$ phosphors under 395 nm excitation displayed the typical emissions in the 560–720 nm region, which correspond to the $^5D_0 \rightarrow {}^7F_J$ (J = 0, 1, 2, 3 and 4) intra-4f shell electronic transitions expected for the Eu^{3+} ion (Fig. 7(b)). It can be observed that the relative emission intensity of $^5D_0 \rightarrow {}^7F_2$ transition was higher than that associated with

$^5D_0 \rightarrow {}^7F_1$ transition, indicating that the Eu^{3+} ion occupies the host lattice without inversion symmetry in the Eu^{3+}-activated BiOBr phosphors.[10] Moreover, the intensity of the emission peaks increase with increasing Eu^{3+} ion concentration.

3.7. CIE chromaticity diagram

For practical lighting applications, color quality was specified in terms of 1931 Commission International de l'Eclairage (CIE) chromaticity color coordinates. These color coordinates recognize that the human visual system uses three primary colors: red, green and blue.[29] In general, the color of any light source can be represented on the (x, y) coordinates in this color space. To evaluate the phosphors performance on color luminescent emission, the Commission International de I'Eclairage (CIE) chromaticity coordinates (x, y) were calculated using the color calculator program radiant imaging.[30] Fig. 8(a) and (b) shows the CIE chromaticity diagram of $Bi_{1-x}Eu_xOF$ and $Bi_{1-x}Eu_xOBr$ phosphors excited at 395 nm. The calculated CIE chromaticity coordinates of $Bi_{1-x}Eu_xOF$ (x = 0.01, 0.03 and 0.05) phosphors were found to be (0.560, 0.439), (0.587, 0.412) and (0.597, 0.402) respectively (Fig. 8(a)). The color coordinates of Eu^{3+}-activated BiOF lies in the orange-red region of CIE chromaticity diagram.[31] This was due to the dominancy of orange emission ($^5D_0 \rightarrow {}^7F_1$) as compared to the red emission ($^5D_0 \rightarrow {}^7F_2$). For $Bi_{1-x}Eu_xOBr$ phosphors, the CIE coordinates were calculated to be (0.602, 0.387), (0.619, 0.370) and (0.632, 0.358) (Fig. 8(b)). The evaluated CIE color coordinates for 5 mol% Eu^{3+}-activated BiOBr (0.632, 0.358) is close to the commercial Y_2O_3:Eu^{3+} (0.645, 0.347) and Y_2O_2S: Eu^{3+} (0.647, 0.343) red phosphors.[32] This indicates that the 5 mol% Eu^{3+}-activated BiOBr is a potential candidate for the development of red component in WLEDs as compared to Eu^{3+}-activated BiOF phosphors.

3.8. Judd–Ofelt intensity parameters and radiative properties

The emission spectra of $Bi_{1-x}Eu_xOX$ phosphors were used for estimation of the Judd–Ofelt (J–O) intensity parameters for Eu^{3+} ion. The Judd–Ofelt intensity parameters ($\Omega_{2,4}$) provide valuable information about the local structure and bonding in the vicinity of rare earth ions. Through these analyses, the local environment around the metal ion and the bond covalency of metal-ligand bonds can be interpreted. The relative integrated emission intensities $I_{^7F_J}$ (J = 0, 1, 2, 3 and 4) for all the $^5D_0 \rightarrow {}^7F_J$ transitions were calculated using the emission spectra of $Bi_{1-x}Eu_xOX$ phosphors. The total relative integrated intensity I $\left(I = \sum_{J=0-4} I_{^7F_J} \right)$ is proportional to the total radiative transition rate $\sum_{J=0-4} A_{^7F_J}$ and is given by:[33]

$$I = a \sum_{J=0-4} A_{^7F_J} \tag{4}$$

where a is a constant and $A_{^7F_J}$ is the radiative transition rate for $^5D_0 \rightarrow {}^7F_J$ transitions. The total radiative transition rate is equal to the reciprocal of experimental lifetime τ and is as follows:

$$\sum_{J=0-4} A_{^7F_J} = \frac{1}{\tau} \tag{5}$$

Fig. 9 shows the PL decay curve for $Bi_{1-x}Eu_xOX$ (X = F and Br) phosphors measured at low temperature (77 K). These decay profiles exhibit single exponential behavior and the excited state lifetime was calculated from the slope of the fitting line using the following expression:

$$I_t = I_0 e^{-t/\tau} \tag{6}$$

where I_t and I_0 are the luminescence intensities at time t and at t = 0 respectively, τ is the lifetime of the excited state energy level. The experimental lifetime (τ) values of the $^5D_0$ level were found to be 3.95 and 4.12 ms for $Bi_{1-x}Eu_xOF$ and $Bi_{1-x}Eu_xOBr$ phosphors, respectively. The obtained lifetime values were found to be larger than Eu^{3+} doped ZnAlBiB,[34] Eu^{3+} doped $KLa(PO_3)_4$,[35] $Sr_{1.7}Zn_{0.3}CeO_4$: Eu^{3+},[2] $Ca_{19}Mg_2(PO_4)_{14}$: Eu^{3+},[36] Eu^{3+}-doped Glaserite-type Orthovanadates $CsK_2Gd[VO_4]_2$,[37] $NaLu(WO_4)_2$:Eu^{3+} [38].

The value of a for $Bi_{1-x}Eu_xOX$ can be obtained from eqn (4). Accordingly, the radiative transition rate $A_{^7F_J}$ for each transition between two manifolds $^5D_0$ and ^7F_J (J = 0, 1, 2, 3 and 4) can be calculated and the values are displayed in Table 3.

The radiative transition rate of $^5D_0 \rightarrow {}^7F_1$ ($A^{md}_{J'-J}$) related to magnetic dipole transition from the initial state J′ to the final state J can be expressed as:[39, 40]

$$A^{md}_{J'-J} = \frac{64\pi^4\nu^3}{3h(2J'+1)} n^3 S_{md} \quad (7)$$

where ν is the wavenumber for J′→J transition, h is Planck's constant (h = 6.626 × 10^{-27} erg s), (2J′ + 1) is the degeneracy of the initial state, n is the refractive index of the host and S_{md} is the magnetic dipole line strength (S_{md} = 7.83 × 10^{-42}). From eqn (7), the refractive index of BiOF and BiOBr hosts can be calculated to be 2.11 and 1.67, respectively.

The radiative transition rates, which were electric dipole transitions and can be written as a function of the J–O intensity parameters:

$$A^{ed}_{J'-J} = \frac{64\pi^4\nu^3e^2}{3h(2J'+1)} \frac{n(n^2+2)^2}{9} \sum_{J=2,4} \Omega_J \left\langle {}^5D_0 \left| U^{(J)} \right| {}^7F_J \right\rangle^2 \quad (8)$$

The $\langle {}^5D_0|U^{(J)}|{}^7F_J\rangle^2$ are the square reduced matrix elements whose values are independent of the chemical environment of the Eu^{3+} ion. Their values were known and are solely $\langle {}^5D_0|U^{(2)}|{}^7F_2\rangle^2$ =

0.0032 and $\langle {}^5D_0|U^{(4)}|{}^7F_4\rangle^2 = 0.0023$. Thus, using eqn (8), the values of J–O intensity parameters ($\Omega_{2,4}$) were obtained.

For $Bi_{1-x}Eu_xOF$ phosphors, Ω_2 and Ω_4 can be deduced to be 0.8775×10^{-20} and 0.5771×10^{-20} cm^2, respectively. It is well known that the Ω_2 parameter was structure sensitive and depends on the covalence of the rare-earth ion sites. The parameter Ω_4 was not directly related to the symmetry of the Eu^{3+} ion but to the electron density on the surrounding ligands. The trend observed in the J–O parameters ($\Omega_2 > \Omega_4$) for $Bi_{1-x}Eu_xOF$ phosphors confirmed the covalency between the metal and ligands. In case of $Bi_{1-x}Eu_xOBr$ phosphors, the value of Ω_4 (3.1559×10^{-20} cm^2) is larger than Ω_2 (1.6206×10^{-20} cm^2) which reveal the less covalent nature of Eu–O bond character.

The branching ratio β corresponding to the emission from an excited level to its lower levels is as follows:

$$\beta = \frac{A_{J'-J}}{\sum_{J=0-4} A_{J'-J}} \tag{9}$$

The branching ratios for the $^5D_0$ level of Eu^{3+} in BiOF and BiOBr are listed in Table 3. In $Bi_{1-x}Eu_xOF$ phosphors, the β value of $^5D_0 \rightarrow {}^7F_1$ emission was higher than the other transitions, indicating that the $^5D_0 \rightarrow {}^7F_1$ transition was the main emission of Eu^{3+} ion. It was observed that the β value of $^5D_0 \rightarrow {}^7F_2$ transition was dominant in $Bi_{1-x}Eu_xOBr$ phosphors.

The stimulated emission cross-section (σ_e) was an essential parameter to signifies the rate of energy extraction from the lasing material and is calculated as

$$\sigma_e(\lambda_P) = \left[\frac{\lambda_P^4}{8\pi c n^2 \Delta\lambda_{eff}}\right] A_{J'-J} \tag{10}$$

where λ_p is the emission peak wavelength, c is the velocity of light and $\Delta\lambda_{eff}$ is the effective bandwidth of the emission transition.

Table 4 illustrates the asymmetry ratios, effective bandwidth of the emission transition ($\Delta\lambda_{eff}$), stimulated emission cross-section (σ_e), gain bandwidth ($\sigma_e \times \Delta\lambda_{eff}$) and optical gain ($\sigma_e \times \tau$) for $Bi_{1-x}Eu_xOX$ phosphors. To understand the variation of symmetry and coordination environment around Eu^{3+} ion doped in BiOX matrices, the asymmetric ratio was calculated. It is the relative intensity ratio of $^5D_0 \rightarrow {}^7F_2$ and $^5D_0 \rightarrow {}^7F_1$ transitions. The low values of asymmetric ratio for $Bi_{1-x}Eu_xOF$ phosphors show that the Eu^{3+} ion occupies site with a high symmetry and with an inversion center (Table 4). In contrast, the high asymmetric ratios revealed that the Eu^{3+} ion has a lack of inversion symmetry in $Bi_{1-x}Eu_xOBr$ phosphors.

The stimulated emission cross-section value is an important factor to predict the laser performance of a material and also the rate of the energy extraction from the lasing material. The trend of σ_e for the $^5D_0$ emission transition were observed as $^7F_1 > {}^7F_2 > {}^7F_4 > {}^7F_3 > {}^7F_0$ ($Bi_{1-x}Eu_xOF$) and $^7F_4 > {}^7F_2 > {}^7F_3 > {}^7F_1 > {}^7F_0$ ($Bi_{1-x}Eu_xOBr$). The stimulated emission cross-section values of Eu^{3+}-activated BiOBr phosphors for $^5D_0 \rightarrow {}^7F_2$ transition were found to be better than Eu^{3+}-activated BiOF phosphors. The product of emission cross-section and the effective bandwidth of the emission transition is a significant parameter to predict the bandwidth of the optical amplifier. The higher the product values were, the better was the amplifiers performance. It was noteworthy that the maximum value of gain bandwidth was 7.42×10^{-28} cm^3 corresponding to $^5D_0 \rightarrow {}^7F_4$ transition for $Bi_{0.99}Eu_{0.01}OBr$ phosphor. Similarly, the product of radiative lifetime and stimulated emission cross section is a vital aspect for high optical amplifier gain. The obtained optical gain value of $Bi_{0.95}Eu_{0.05}OBr$ phosphor corresponding to $^5D_0 \rightarrow {}^7F_2$ transition were found to be larger than Eu^{3+} doped ZnAlBiB[34] and Eu^{3+} doped $KLa(PO_3)_4$[35]. Therefore, we

can conclude that the Eu^{3+}-activated BiOBr phosphors corresponding to $^5D_0 \rightarrow {}^7F_2$ transition provide favorable lasing action, high optical gain for amplifiers and can be useful for red laser applications.

3.9. Photocatalytic activity

The temporal evolution of photocatalytic degradation of aqueous RhB dye solution over $Bi_{1-x}Eu_xOF$ and $Bi_{1-x}Eu_xOBr$ catalysts under visible light irradiation are shown in Figs. S6 and S7, respectively. All the spectra show characteristic absorption peak of RhB at 554 nm whose intensity decreased dramatically as a function of irradiation time in the presence of the photocatalysts. Further, visible light irradiation of the aqueous RhB/$Bi_{1-x}Eu_xOX$ dispersion leads to a concomitant wavelength shift of the band to lower wavelengths. The blue shift depicted in Figs. S6 and S7 were caused by de-ethylation of RhB due to an attack by one of the active oxygen species on the N-ethyl group. The shifting of the maximum absorption of RhB dye to other wavelength positions of its major absorption band which moved toward the N,N,N'-tri-ethylated rhodamine (λ_{max} = 539 nm); N,N'-di-ethylated rhodamine, (λ_{max} = 522 nm) and rhodamine (λ_{max} = 498 nm) species.[41] The intensity of the main peak reduced gradually to zero within 75 and 20 min over $Bi_{1-x}Eu_xOF$ and $Bi_{1-x}Eu_xOBr$ catalysts, respectively. Fig. 10(a) and (b) shows the percentage of RhB dye degradation mediated by $Bi_{1-x}Eu_xOX$ (X = F and Br) catalysts with irradiation time. The adsorption-desorption equilibrium between RhB and catalysts can be established within 30 min (dark condition), and at most 46% and 60% of the RhB dye degradation was observed for $Bi_{1-x}Eu_xOF$ and $Bi_{1-x}Eu_xOBr$ catalysts, respectively. This revealed that $Bi_{1-x}Eu_xOBr$ catalysts have good adsorption capacity. The 100% RhB dye was decomposed within 75 and 20 min over $Bi_{1-x}Eu_xOX$ (X = F and Br) catalysts under visible illumination.

To prove the efficiency of $Bi_{1-x}Eu_xOX$ catalysts with the possibility for future industrial applications, the reaction kinetics was evaluated. The RhB dye degradation follows apparent first order kinetics, in agreement with a general Langmuir–Hinshelwood mechanism[42]

$$R = \frac{-dC}{dt} = \frac{kKC}{1+KC} \quad (11)$$

where R is the degradation rate of reactant (mg/l min), C is the concentration of reactant (mg/l), t is the illumination time, K is the adsorption coefficient of reactant (l/mg) and k is the reaction rate constant. If C is very small then the above equation could be simplified to

$$\ln\left(\frac{C_0}{C}\right) = kKt = k_{app}t \quad (12)$$

where C_0 is the initial concentration (0 min) of the RhB aqueous solution and C is the concentration of the RhB aqueous solution for different times of visible illumination.

According to eqn (12), if $\ln(C_0/C)$ was plotted as a function of t , a straight line was observed, whose slope is equal to the apparent first-order rate constant k_{app} which were calculated to be 0.04206 and 0.20792 min^{-1} for BiOF and BiOBr catalysts, respectively (Fig. 11). These values substantiate the photocatalytic reaction rate being highest for BiOBr catalyst. Further, the rate constants decrease with increasing Eu^{3+} ion concentration in BiOX. This was due to the increase in band gap energy values with increase in Eu^{3+} concentration.

We have also compared our photocatalytic results with the reported catalysts synthesized by different methods for the degradation of RhB dye under visible light irradiation and are shown in Table 5. The table reveals that BiOBr catalyst synthesized by solid state method shows 100% RhB dye degradation in shorter duration (20 min.) and its rate constant is higher as

compared to BiOCl,[18,24] BiOBr/montmorillonite,[20] 1 wt% g-C_3N_4/BiOBr,[22] Fe_3O_4/BiOCl,[43] MnO_x/BiOI,[44] N-doped $BaTiO_3$,[45] Ag_3PO_4[46] and $Bi_2O_2CO_3$[47] catalysts. It is well known that photocatalysts in decomposition of organic pollutants would mostly rely on the utilization of sunlight energy and the efficiency of photogenerated charge carriers. Moreover, the band gap energy, optical transition and structure of materials were the influencing factors for photogenerated free-carrier's generation, capture, transport and separation. The indirect optical transition of BiOBr plays a significant role in its excellent photocatalytic activity as compared to direct transition of BiOF. In indirect transition, an excited electron has to travel certain k-space distance to reach valence band. This reduces the recombination probability of the excited electron and the hole. Compared to BiOF photocatalyst, BiOBr can absorb more photons to achieve the electron-excited process due to its smaller band gap. As a result of this, more hydroxyl radicals or holes may be produced under the visible light irradiation. The layered structure of BiOX can polarize the related atoms and orbitals by supporting large enough space,[48] resulting in an increase in the electron–hole separation efficiency through the appeared dipole, and thus the enhanced photocatalytic activity was observed.

4. Conclusions

Eu^{3+}-activated BiOX (X = F and Br) phosphors have been synthesized and their structural parameters were evaluated. Based on the CIE chromaticity diagram, the Eu^{3+}-activated BiOF phosphors exhibit orange-red luminescence. In contrast, the Eu^{3+}-activated BiOBr phosphors illustrate red luminescence. The CIE coordinates of $Bi_{0.95}Eu_{0.05}OBr$ phosphor is close to the commercial Y_2O_3:Eu^{3+} and Y_2O_2S: Eu^{3+} red phosphors. From the Judd–Ofelt analysis, we observed that the intensity parameter, Ω_2 was greater than Ω_4 for $Bi_{1-x}Eu_xOF$ phosphors which suggest the more covalency from the metal (Eu) to ligands (O). In case of $Bi_{1-x}Eu_xOBr$

phosphors, Ω_2 was less than Ω_4 which reveal the less covalent nature of Eu–O bond character. The asymmetry ratio for $Bi_{1-x}Eu_xOF$ phosphors confirmed that Eu^{3+} ion was located at site with inversion symmetry, whereas Eu^{3+} ion occupies the site without inversion symmetry in the BiOBr host lattice. The $Bi_{0.95}Eu_{0.05}OBr$ phosphor shows long lifetime and higher optical gain parameter for $^5D_0 \rightarrow {}^7F_2$ transition in comparison with reported Eu^{3+} doped host matrices. Under visible illumination, 100% RhB dye was degraded within 75 minutes ($Bi_{1-x}Eu_xOF$) and 20 minutes ($Bi_{1-x}Eu_xOBr$). These results suggest that BiOBr is a good host material to incorporate the lanthanide ions for exhibiting good luminescence properties as well as photocatalytic activity for energy and environmental sustainability applications.

References

1 C. C. Wu, K. B. Chen, C. S. Lee, T. M. Chen and B. M. Cheng, *Chem. Mater.*, 2007, **19**, 3278–3285.

2 H. Li, R. Zhao, Y. Jia, W. Sun, J. Fu, L. Jiang, S. Zhang, R. Pang and C. Li, *ACS Appl. Mater. Interfaces*, 2014, **6**, 3163–3169.

3 T. Hase, T. Kano, E. Nakazawa and H. Yamamoto, *Adv. Electron El. Phys.*, 1990, **79**, 271–373.

4 M. M. Shang, G. G. Li, X. J. Kang, D. M. Yang, D. L. Geng, C. Peng, Z. Y. Cheng, H. Z. Lian and J. Lin, *Dalton Trans.*, 2012, **41**, 5571–5580.

5 B. Wu, Q. Zhang, H. Wang and Y. Li, *Cryst. Eng. Comm.*, 2012, **14**, 2094–2099.

6 A. Dash, S. Sarkar, V. N. Adusumalli and V. Mahalingam, *Langmuir*, 2014, **30**, 1401–1409.

7 R. Saraf, C. Shivakumara, N. Dhananjaya, S. Behera and H. Nagabhushana, *J. Mater. Sci.*, 2015, **50**, 287–298.

8 R. Y. Yang, Y. M. Peng, H. L. Lai, C. J. Chu, B. Chiou and Y. K. Su, *Opt. mater.*, 2013, **35**, 1719–1723.

9 L. Han, L. Zhao, J. Zhang, Y. Wang, L. Guo and Y. Wang, *RSC Adv.*, 2013, **3**, 21824– 21831.

10 J. Yu, K. Huang, L. Yuan and S. Feng, *New J. Chem.*, 2014, **38**, 1441–1445.

11 K. Matsui, M. Arima and H. Kanno, *Opt. mater.*, 2013, **35**, 1947–1951.

12 Q. Wu, Y. Li, X. Wang, Z. Zhao, C. Wang, H. Li, A. Mao and Y. Wang, *RSC Adv.*, 2014, **4**, 39030–39036.

13 S. Som, P. Mitra, V. Kumar , V. Kumar, J. J. Terblans, H. C. Swart and S. K. Sharma, *Dalton Trans.*, 2014, **43**, 9860–9871.

14 G. G. Briand and N. Burford, *Chem. Rev.*, 1999, **99**, 2601–2658.

15 S. K. Poznya, *Electrochim. Acta*, 1990, **35**, 1941–1947.

16 C. H. Wang, C. L. Shao, Y. C. Liu and L. N. Zhang, *Scr. Mater.*, 2008, **59**, 332–335.

17 S. J. Wu, C. Wang, Y. F. Cui, T. M. Wang, B. B. Huang, X. Y. Zhang, X. Y. Qin and P. Brault, *Mater. Lett.*, 2010, **64**, 115–118.

18 L. Chen, S. F. Yin, R. Huang, Y. Zhou, S. L. Luo and C. T. Au, *Catal. Commun.*, 2012, **23**, 54–57.

19 D. Zhang, J. Li, Q. G. Wang and Q. S. Wu, *J. Mater. Chem. A*, 2013, **1**, 8622–8629.

20 C. Xu, H. Wu and F. L. Gu, *J. Hazard. Mater.*, 2014, **275**, 185–192.

21 D. H. Wang, G. Q. Gao, Y. W. Zhang, L. S. Zhou, A. W. Xu and W. Chen, *Nanoscale*, 2012, **4**, 7780–7785.

22 J. Xia, J. Di, S. Yin, H. Li, H. Xu, L. Xu, H. Shu and M. He, *Mat. Sci. Semicon. Proc.*, 2014, **24**, 96–103.

23 C. H. Deng and H. M. Guan, *Mater. Lett.*, 2013, **107**, 119–122.

24 J. Y. Xiong, Z. B. Jiao, G. X. Lu, W. Ren, J. H. Ye and Y. P. Bi, *Chem.–Eur. J.*, 2013, **19**, 9472–9475.

25 Y. Q. Lei, G. H. Wang, S. Y. Song, W. Q. Fan and H. J. Zhang, *Cryst. Eng. Comm.*, 2009, **11**, 1857–1862.

26 J. Tauc, *Optical Properties of Solids*, North-Holland, Amsterdam, 1970.

27 W. L. Huang and Q. Zhu, *Comp. Mater. Sci.*, 2008, **43**, 1101–1108.

28 W. Zhang, Q. Zhang and F. Dong, *Ind. Eng. Chem. Res.*, 2013, **52**, 6740–6746.

29 S. Shionoya and W. M. Yen, *Phosphor Handbook, Phosphor Research Society*, CRC Press, 1998.

30 Color Calculator version 2, *A software from Radiant Imaging*, Inc, 2007.

31 A. Escudero, E. Moretti and M. Ocaña, *Cryst. Eng. Comm.*, 2014, **16**, 3274–3283.

32 C. H. Huang, T. W. Kuo and T. M. Chen, *Opt. Express*, 2011, **19**, A1–A6.

33 B. Tian, B. Chen, Y. Tian, X. Li, J. Zhang, J. Sun, H. Zhong, L. Cheng, S. Fu, H. Zhong, Y. Wang, X. Zhang, H. Xia and R. Hua, *J. Mater. Chem. C*, 2013, **1**, 2338–2344.

34 K. Swapna, S. Mahamuda, A. S. Rao, T. Sasikala, P. Packiyaraj, L. R. Moorthy and G. V. Prakash, *J. Lumin.*, 2014, **156**, 80–86.

35 M. Ferhi, C. Bouzidi, K. H. Naifer, H. Elhouichet and M. Ferid, *J. Lumin.*, 2015, **157**, 21–27.

36 G. Zhu, Z. Ci, Y. Shi, M. Que, Q. Wang and Y. Wang, *J. Mater. Chem. C*, 2013, **1**, 5960–5969.

37 Z. Tao, T. Tsuboi, Y. Huang, W. Huang, P. Cai and H. J. Seo, *Inorg. Chem.*, 2014, **53**, 4161–4168.

38 Z. Wang, J. Zhong, H. Jiang, J. Wang and H. Liang, *Cryst. Growth Des.*, 2014, **14**, 3767–3773.

39 B. R. Judd, *Phys. Rev.*, 1962, **127**, 750–761.

40 G. S. Ofelt, *J. Chem. Phys.*, 1962, **37**, 511–519.

41 R. Saraf, C. Shivakumara, S. Behera, H. Nagabhushana, and N. Dhananjaya, *RSC Adv.*, 2014, DOI: 10.1039/c4ra10163d.

42 D. F. Ollis, *J. Phys. Chem. B*, 2005, **109**, 2439–2444.

43 L. Zhang, W. Z. Wang, L. Zhou, M. Shang and S. M. Sun, *Appl. Catal., B*, 2009, **90**, 458–462.

44 L. Q. Ye, X. D. Liu, Q. Zhao, H. Q. Xie and L. Zan, *J. Mater. Chem. A*, 2013, **1**, 8978–8983.

45 J. Cao, Y. Ji, C. Tian and Z. Yi, *J. Alloy Compd.*, 2014, **615**, 243–248.

46 T. A. Vu, C. D. Dao, T. T. T. Hoang, K. T. Nguyen, G. H. Le, P. T. Dang, H. T. K. Tran and T. V. Nguyen, *Mater. Lett.*, 2013, **92**, 57–60.

47 P. Madhusudan, J. Zhang, B. Cheng and G. Liu, *Cryst. Eng. Comm.*, 2013, **15**, 231–240.

48 Z. Y. Zhao and W. W. Dai, *Inorg. Chem.*, 2014, DOI: 10.1021/ic5021059.

Figure captions

Fig. 1. XRD patterns of (a) $Bi_{1-x}Eu_xOF$ and (b) $Bi_{1-x}Eu_xOBr$ compounds.

Fig. 2. Observed, calculated and the difference XRD patterns of (a) BiOF, (b) $Bi_{0.95}Eu_{0.05}OF$, (c) BiOBr and (d) $Bi_{0.95}Eu_{0.05}OBr$ compounds.

Fig. 3. SEM micrographs of (a) BiOF, (b) $Bi_{0.95}Eu_{0.05}OF$, (c) BiOBr and (d) $Bi_{0.95}Eu_{0.05}OBr$ compounds.

Fig. 4. FTIR spectra of (a) $Bi_{1-x}Eu_xOF$ and (b) $Bi_{1-x}Eu_xOBr$ compounds.

Fig. 5. UV-Vis absorption spectra of (a) $Bi_{1-x}Eu_xOF$ (Inset shows plots of $(\alpha hv)^2$ vs hν) and (b) $Bi_{1-x}Eu_xOBr$ (Inset shows plots of $(\alpha hv)^{1/2}$ vs hν) compounds.

Fig. 6. (a) Excitation spectrum of $Bi_{0.99}Eu_{0.01}OF$ phosphor and (b) emission spectra of $Bi_{1-x}Eu_xOF$ phosphors.

Fig. 7. (a) Excitation spectrum of $Bi_{0.99}Eu_{0.01}OBr$ phosphor and (b) emission spectra of $Bi_{1-x}Eu_xOBr$ phosphors.

Fig. 8. CIE 1931chromaticity diagram of (a) $Bi_{1-x}Eu_xOF$ and (b) $Bi_{1-x}Eu_xOBr$ phosphors.

Fig. 9. Photoluminescence decay curve for (a) $Bi_{1-x}Eu_xOF$ and (b) $Bi_{1-x}Eu_xOBr$ phosphors measured at 77 K. The solid line gives the exponential fitting result of $Bi_{0.95}Eu_{0.05}OX$ phosphors.

Fig. 10. Percentage of RhB dye degradation as a function of time over (a) $Bi_{1-x}Eu_xOF$ and (b) $Bi_{1-x}Eu_xOBr$ catalysts.

Fig. 11. First order kinetics of RhB dye degradation over (a) $Bi_{1-x}Eu_xOF$ and (b) $Bi_{1-x}Eu_xOBr$ catalysts as a function of irradiation time.

Table 1. Rietveld refined structural parameters for $Bi_{1-x}Eu_xOF$ compounds.

Compounds	BiOF	$Bi_{0.99}Eu_{0.01}OF$	$Bi_{0.97}Eu_{0.03}OF$	$Bi_{0.95}Eu_{0.05}OF$
Crystal System	Tetragonal	Tetragonal	Tetragonal	Tetragonal
Space group	*P4/nmm* (No. 129)	*P4/nmm* (No. 129)	*P4/nmm* (No. 129)	*P4/nmm* (No. 129)
Lattice Parameters				
a (Å)	3.752(3)	3.753(5)	3.753(3)	3.752(5)
c (Å)	6.227(1)	6.229(6)	6.228(4)	6.227(7)
Cell volume ($Å^3$)	87.66(2)	87.76(9)	87.71(8)	87.67(2)
Atomic positions				
Bi/Eu (2c)				
x	0.2500	0.2500	0.2500	0.2500
y	0.2500	0.2500	0.2500	0.2500
z	0.2087(3)	0.2085(3)	0.2091(2)	0.2097(3)
O (2a)				
x	0.2500	0.2500	0.2500	0.2500
y	0.7500	0.7500	0.7500	0.7500
z	0.0000	0.0000	0.0000	0.0000
F (2c)				
x	0.2500	0.2500	0.2500	0.2500
y	0.2500	0.2500	0.2500	0.2500
z	0.6402(3)	0.6427(4)	0.6471(5)	0.6456(3)
***R* Factors**				
R_p	0.091	0.104	0.107	0.100
R_{wp}	0.131	0.141	0.144	0.138
R_{exp}	0.109	0.126	0.124	0.119
χ^2	0.014	0.013	0.013	0.013
R_{Bragg}	0.057	0.071	0.064	0.065
R_F	0.040	0.041	0.036	0.038

Table 2. Rietveld refined structural parameters for $Bi_{1-x}Eu_xOBr$ compounds.

Compounds	BiOBr	$Bi_{0.99}Eu_{0.01}OBr$	$Bi_{0.97}Eu_{0.03}OBr$	$Bi_{0.95}Eu_{0.05}OBr$
Crystal System	Tetragonal	Tetragonal	Tetragonal	Tetragonal
Space group	*P4/nmm* (No. 129)	*P4/nmm* (No. 129)	*P4/nmm* (No. 129)	*P4/nmm* (No. 129)
Lattice Parameters				
a (Å)	3.928(4)	3.928(2)	3.927(4)	3.929(5)
c (Å)	8.108(6)	8.108(3)	8.106(5)	8.111(8)
Cell volume ($Å^3$)	125.09(2)	125.13(2)	125.04(1)	125.19(2)
Atomic positions				
Bi/Eu (2c)				
x	0.2500	0.2500	0.2500	0.2500
y	0.2500	0.2500	0.2500	0.2500
z	0.1565(2)	0.1551(4)	0.1542(7)	0.1562(4)
O (2a)				
x	0.2500	0.2500	0.2500	0.2500
y	0.7500	0.7500	0.7500	0.7500
z	0.0000	0.0000	0.0000	0.0000
Br (2c)				
x	0.2500	0.2500	0.2500	0.2500
y	0.2500	0.2500	0.2500	0.2500
z	0.6496(9)	0.6526(8)	0.6561(8)	0.6513(9)
***R* Factors**				
R_p	0.122	0.127	0.112	0.113
R_{wp}	0.167	0.174	0.158	0.157
R_{exp}	0.147	0.155	0.138	0.136
χ^2	0.013	0.012	0.013	0.013
R_{Bragg}	0.084	0.084	0.064	0.068
R_F	0.060	0.056	0.049	0.051

Table 3. Calculated wavenumbers, transition rates and branching ratios for $^5D_0 \rightarrow {}^7F_J$ (J = 0, 1, 2, 3 and 4) transitions of Eu^{3+} in BiOF and BiOBr.

Compounds	Transition	Type	Wavenumber (cm^{-1})	Transition rate (s^{-1})	β (%)
BiOF: Eu^{3+}	$^5D_0 \rightarrow {}^7F_0$	Forbidden	17271.16	17.01	6.73
	$^5D_0 \rightarrow {}^7F_1$	Magnetic dipole	16891.89	110.61	43.75
	$^5D_0 \rightarrow {}^7F_2$	Electric dipole	16207.46	84.14	33.28
	$^5D_0 \rightarrow {}^7F_3$	Forbidden	15432.10	13.61	5.38
	$^5D_0 \rightarrow {}^7F_4$	Electric dipole	14326.65	27.47	10.86
BiOBr: Eu^{3+}	$^5D_0 \rightarrow {}^7F_0$	Forbidden	17271.16	23.88	9.84
	$^5D_0 \rightarrow {}^7F_1$	Magnetic dipole	16949.15	54.77	22.56
	$^5D_0 \rightarrow {}^7F_2$	Electric dipole	16286.64	68.75	28.32
	$^5D_0 \rightarrow {}^7F_3$	Forbidden	15455.95	30.43	12.53
	$^5D_0 \rightarrow {}^7F_4$	Electric dipole	14285.71	64.94	26.75

Table 4. Asymmetry ratios, effective bandwidth of the emission transition ($\Delta\lambda_{eff}$), stimulated emission cross-section (σ_e), gain bandwidth ($\sigma_e \times \Delta\lambda_{eff}$) and optical gain ($\sigma_e \times \tau_{rad}$) for $Bi_{1-x}Eu_xOX$ phosphors.

Compounds	Transitions	Asymmetry ratio	$\Delta\lambda_{eff}$ (nm)	σ_e ($\times 10^{-22}$ cm^2)	$\sigma_e \times \Delta\lambda_{eff}$ ($\times 10^{-28}$ cm^3)	$\sigma_e \times \tau_{rad}$ ($\times 10^{-25}$ cm^2s^{-1})
$Bi_{0.99}Eu_{0.01}OF$	$^5D_0 \rightarrow {}^7F_0$	0.766	7.00	0.81	0.57	3.20
	$^5D_0 \rightarrow {}^7F_1$		8.10	4.99	4.04	19.71
	$^5D_0 \rightarrow {}^7F_2$		7.77	4.68	3.64	18.49
	$^5D_0 \rightarrow {}^7F_3$		5.94	1.20	0.71	4.74
	$^5D_0 \rightarrow {}^7F_4$		14.00	1.39	1.95	5.49
$Bi_{0.97}Eu_{0.03}OF$	$^5D_0 \rightarrow {}^7F_0$	0.789	5.79	0.98	0.57	3.87
	$^5D_0 \rightarrow {}^7F_1$		7.68	5.27	4.05	20.82
	$^5D_0 \rightarrow {}^7F_2$		8.14	4.46	3.63	17.62
	$^5D_0 \rightarrow {}^7F_3$		6.21	1.15	0.71	4.54
	$^5D_0 \rightarrow {}^7F_4$		9.51	2.04	1.94	8.06
$Bi_{0.95}Eu_{0.05}OF$	$^5D_0 \rightarrow {}^7F_0$	0.760	5.12	1.11	0.57	4.38
	$^5D_0 \rightarrow {}^7F_1$		8.39	4.82	4.04	19.04
	$^5D_0 \rightarrow {}^7F_2$		9.24	3.93	3.63	15.52
	$^5D_0 \rightarrow {}^7F_3$		6.46	1.13	0.73	4.46
	$^5D_0 \rightarrow {}^7F_4$		7.13	2.72	1.94	10.74
$Bi_{0.99}Eu_{0.01}OBr$	$^5D_0 \rightarrow {}^7F_0$	1.42	9.00	1.42	1.28	5.85
	$^5D_0 \rightarrow {}^7F_1$		11.14	2.83	3.15	11.66
	$^5D_0 \rightarrow {}^7F_2$		10.31	4.51	4.65	18.58
	$^5D_0 \rightarrow {}^7F_3$		7.21	3.52	2.54	14.50
	$^5D_0 \rightarrow {}^7F_4$		12.09	6.14	7.42	25.30
$Bi_{0.97}Eu_{0.03}OBr$	$^5D_0 \rightarrow {}^7F_0$	1.36	8.00	1.60	1.28	6.59
	$^5D_0 \rightarrow {}^7F_1$		12.82	2.46	3.15	10.13
	$^5D_0 \rightarrow {}^7F_2$		7.22	6.44	4.65	26.53
	$^5D_0 \rightarrow {}^7F_3$		7.48	3.39	2.54	13.97
	$^5D_0 \rightarrow {}^7F_4$		10.97	6.76	7.41	27.85
$Bi_{0.95}Eu_{0.05}OBr$	$^5D_0 \rightarrow {}^7F_0$	1.27	10.00	1.28	1.28	5.27
	$^5D_0 \rightarrow {}^7F_1$		10.53	3.00	3.16	12.36
	$^5D_0 \rightarrow {}^7F_2$		6.35	7.32	4.64	30.16
	$^5D_0 \rightarrow {}^7F_3$		6.89	3.68	2.53	15.16
	$^5D_0 \rightarrow {}^7F_4$		8.51	8.71	7.41	35.88

Table 5. Comparison of BiOX (X = F and Br) catalysts with the reported catalysts for RhB dye degradation.

Catalyst	Synthesis method	Initial RhB conc.	Catalyst conc. (mg/L)	Reaction condition (Visible)	RhB degradation		Rate constant (min^{-1})	Ref.
					%	Time taken (min.)		
BiOCl	Hydrolysis	10 mg/L	500	250 W	100	50	0.1186	[18]
BiOBr/montmorillonite	Hydro-thermal	40 mg/L	1000	1000 W	99	120	-	[20]
1 wt% g-C_3N_4/BiOBr	Solvo-thermal	10 mg/L	200	300 W	100	150	-	[22]
BiOCl	Solution oxidation	1×10^{-5} M	100	300 W	100	80	-	[24]
Fe_3O_4/BiOCl	Phase-transfer	30 mg/L	1000	500 W	100	40	0.066	[43]
MnO_x/BiOI	Photo-deposition	5 mg/L	200	500 W	78.8	30	-	[44]
N-doped $BaTiO_3$	Melt salt	10 mg/L	1000	300W	48	240	0.00281	[45]
Ag_3PO_4	Precipitation	15 mg/L	300	15 W	96	180	-	[46]
$Bi_2O_2CO_3$	Hydro-thermal	1×10^{-5} M	5000	350 W	95	90	0.0506	[47]
BiOF	Solid state	1×10^{-5} M	1000	500 W	100	75	0.04206	Present work
BiOBr	Solid state	1×10^{-5} M	1000	500 W	100	20	0.20792	Present work

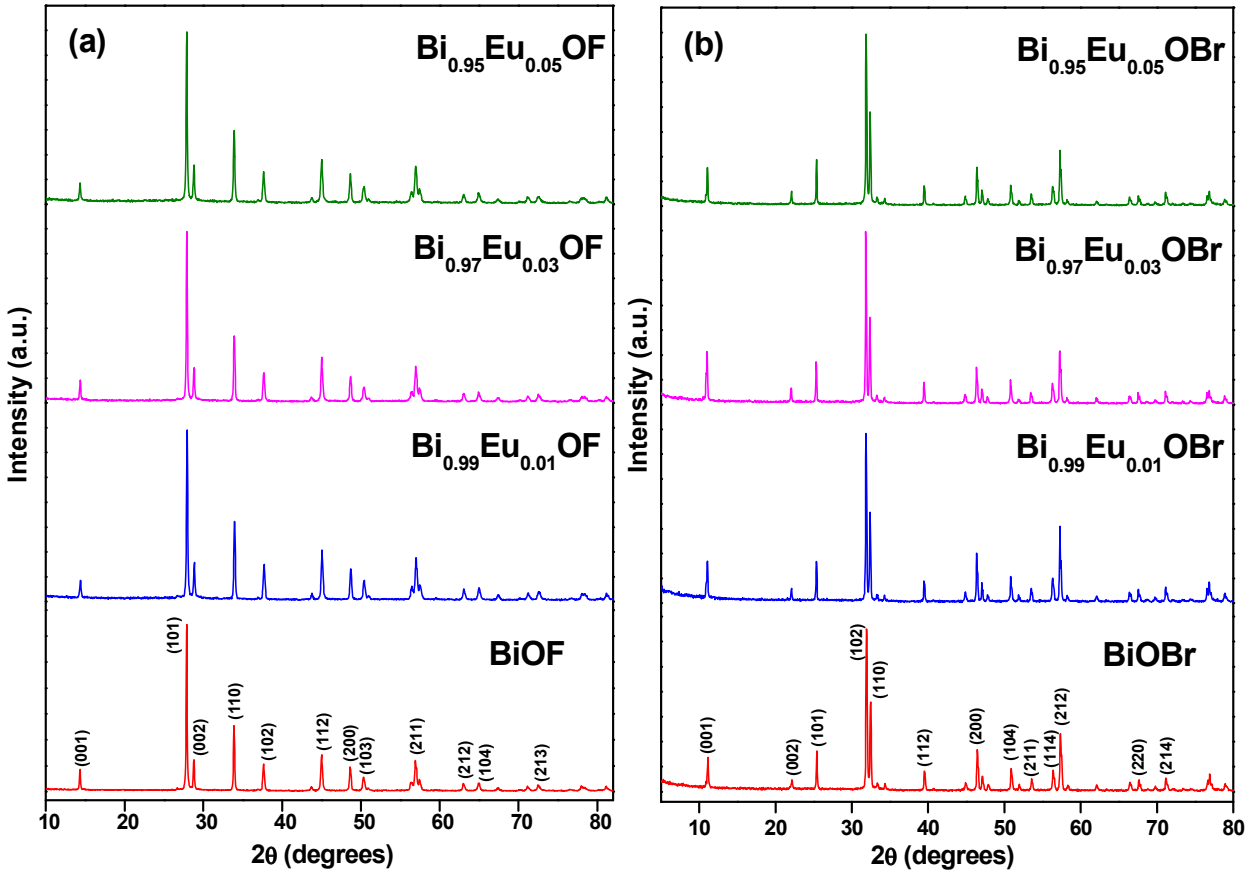

Fig. 1

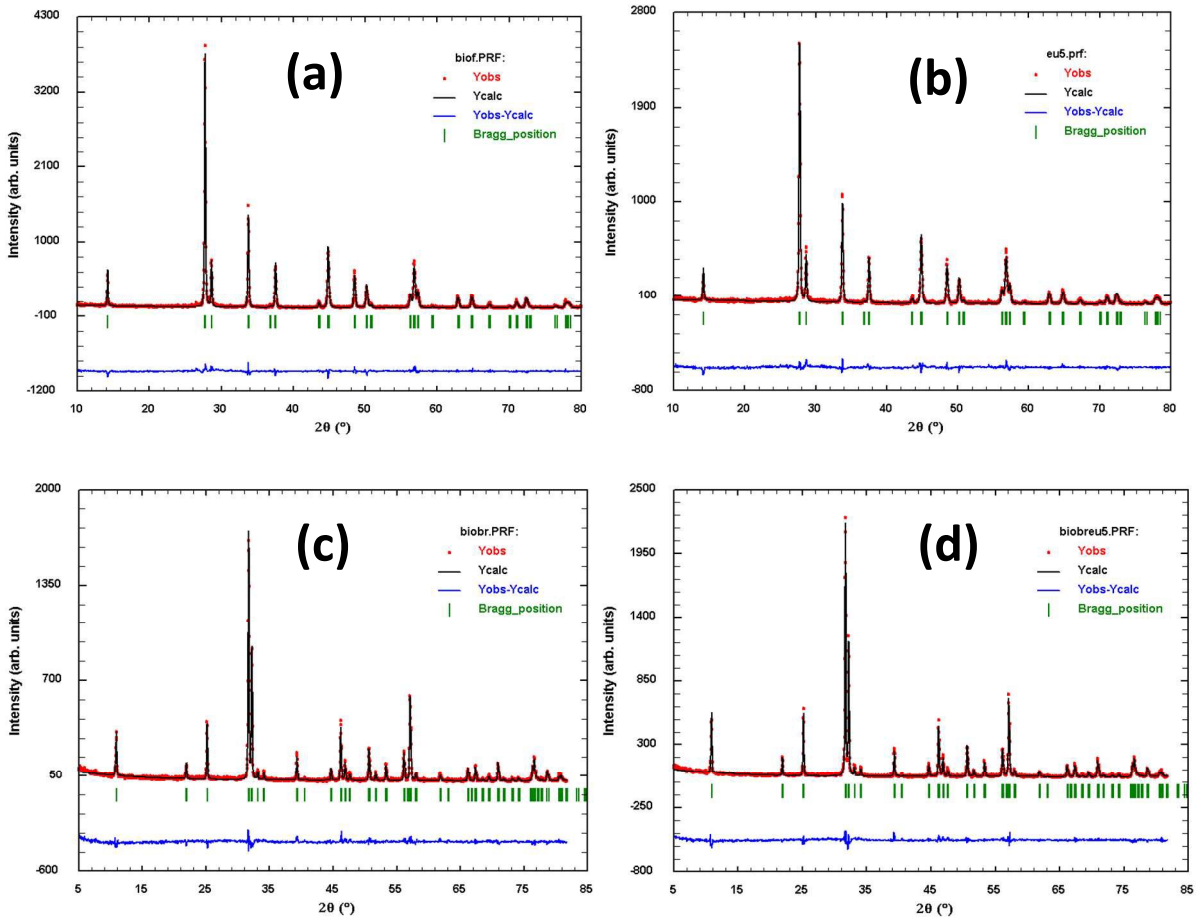

Fig. 2

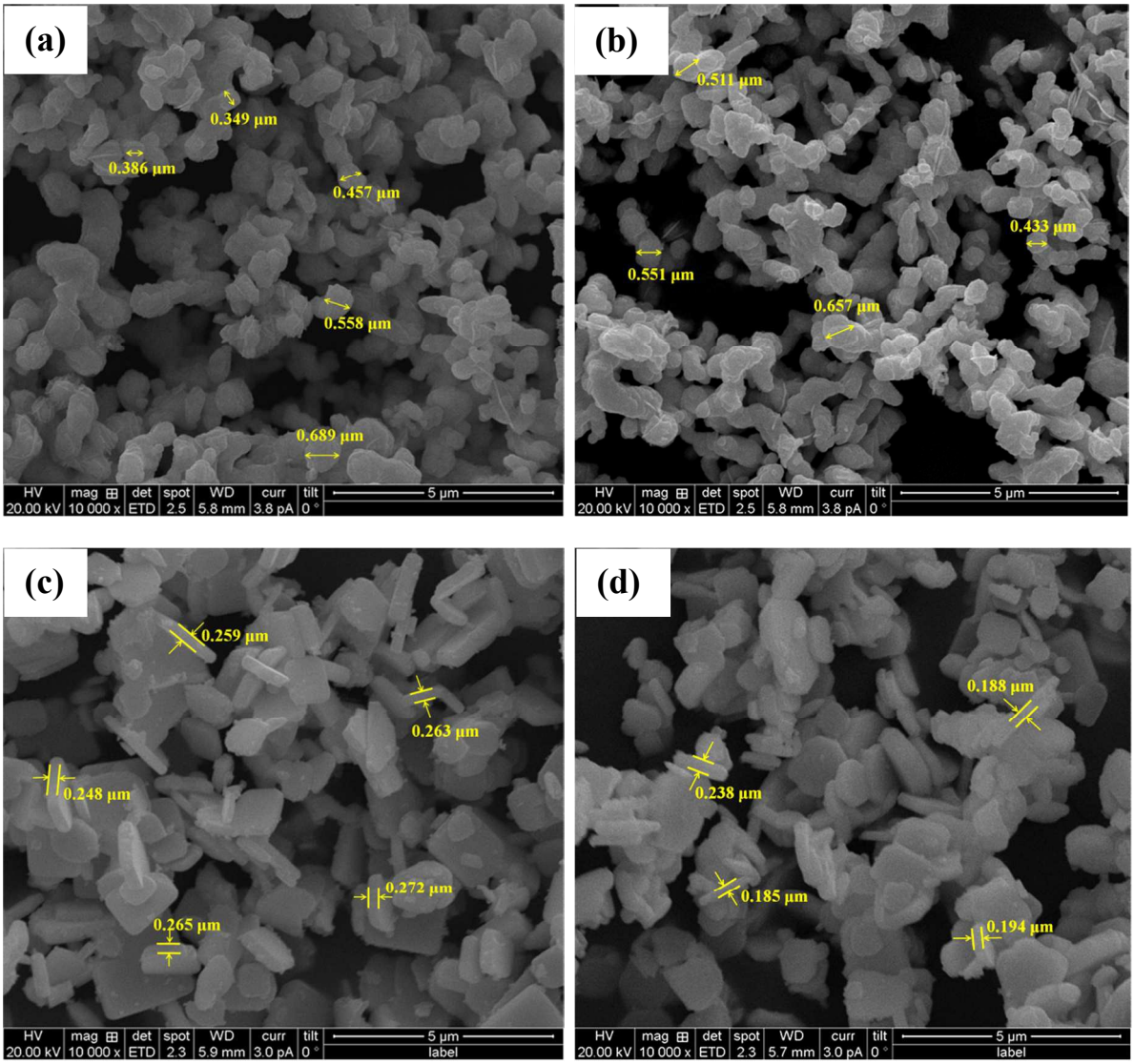

Fig. 3

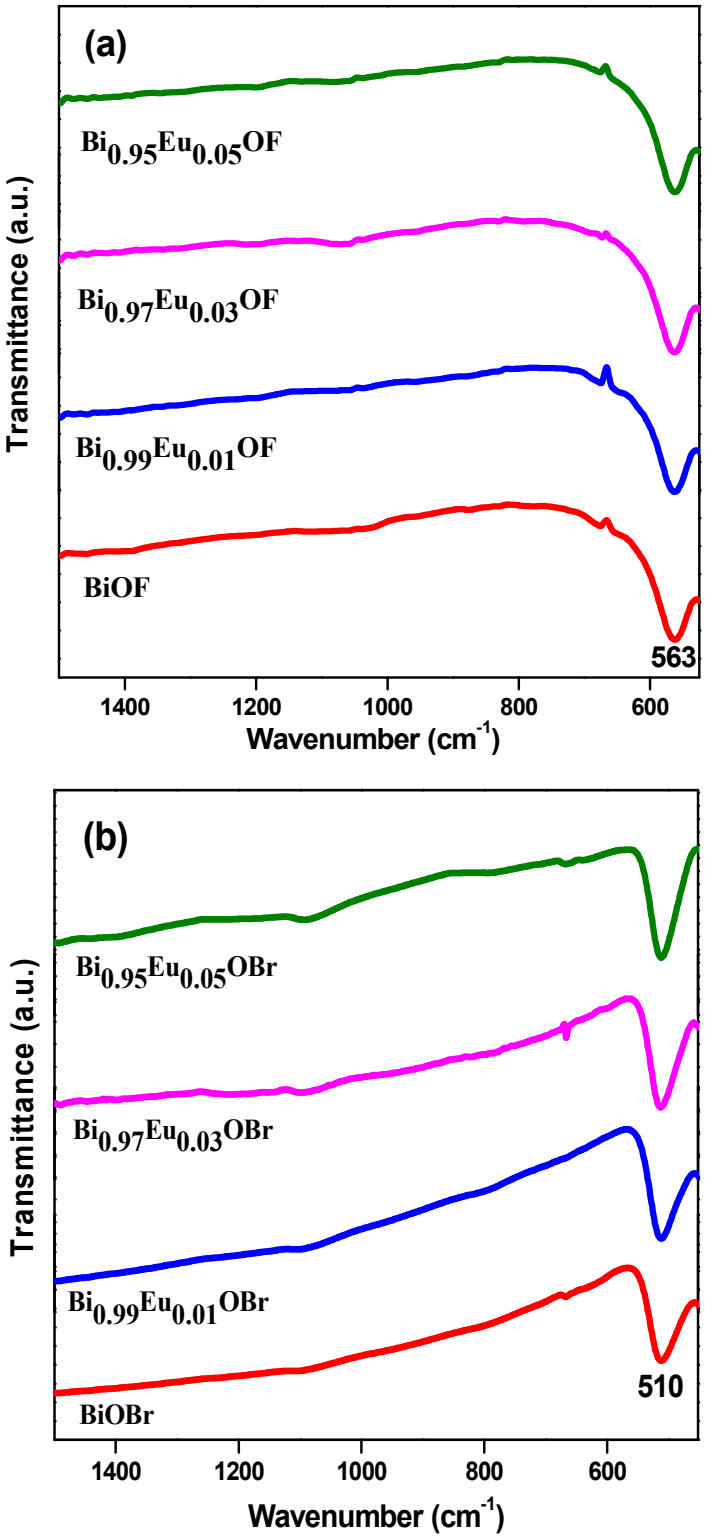

Fig. 4

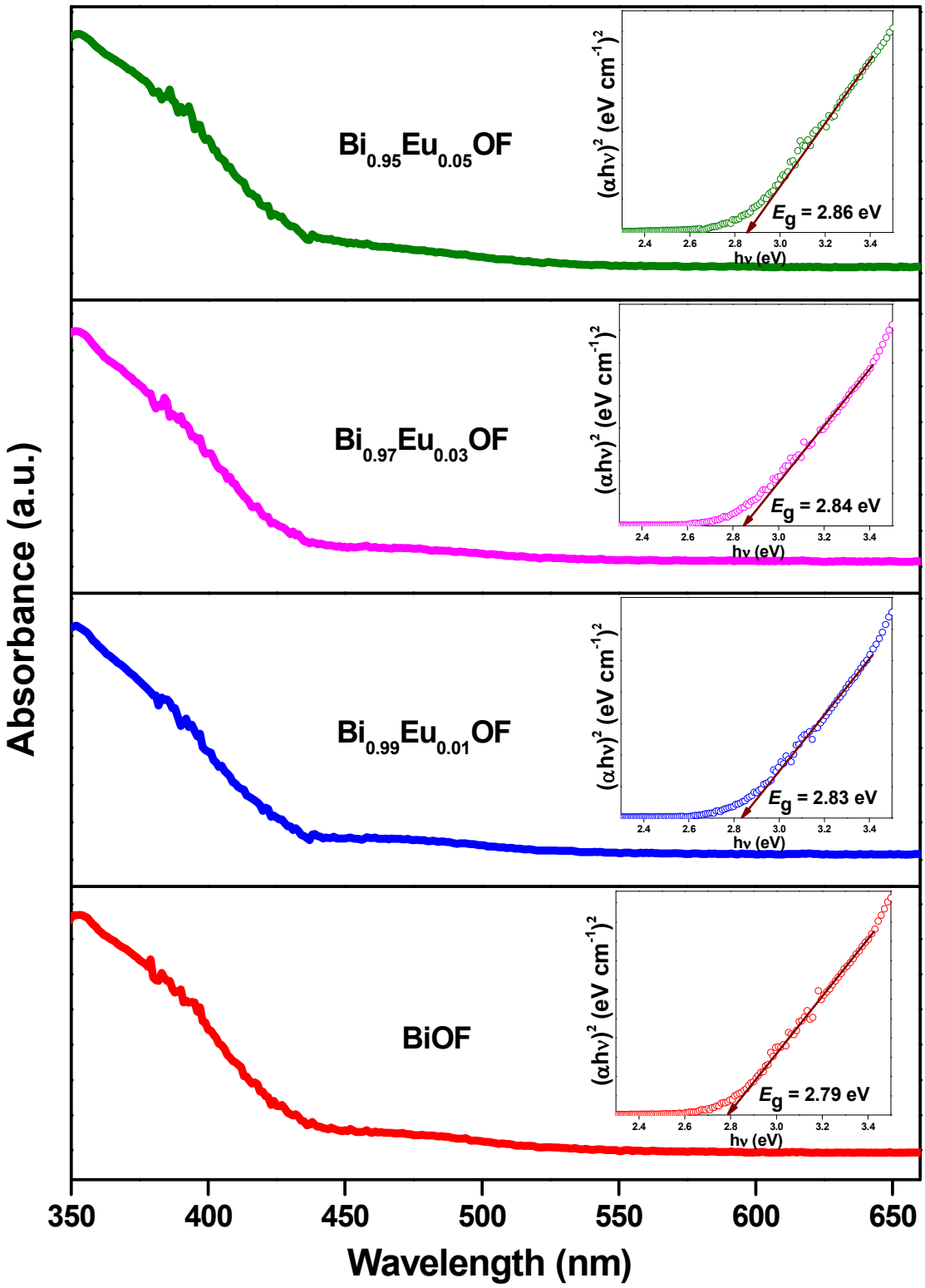

Fig. 5(a)

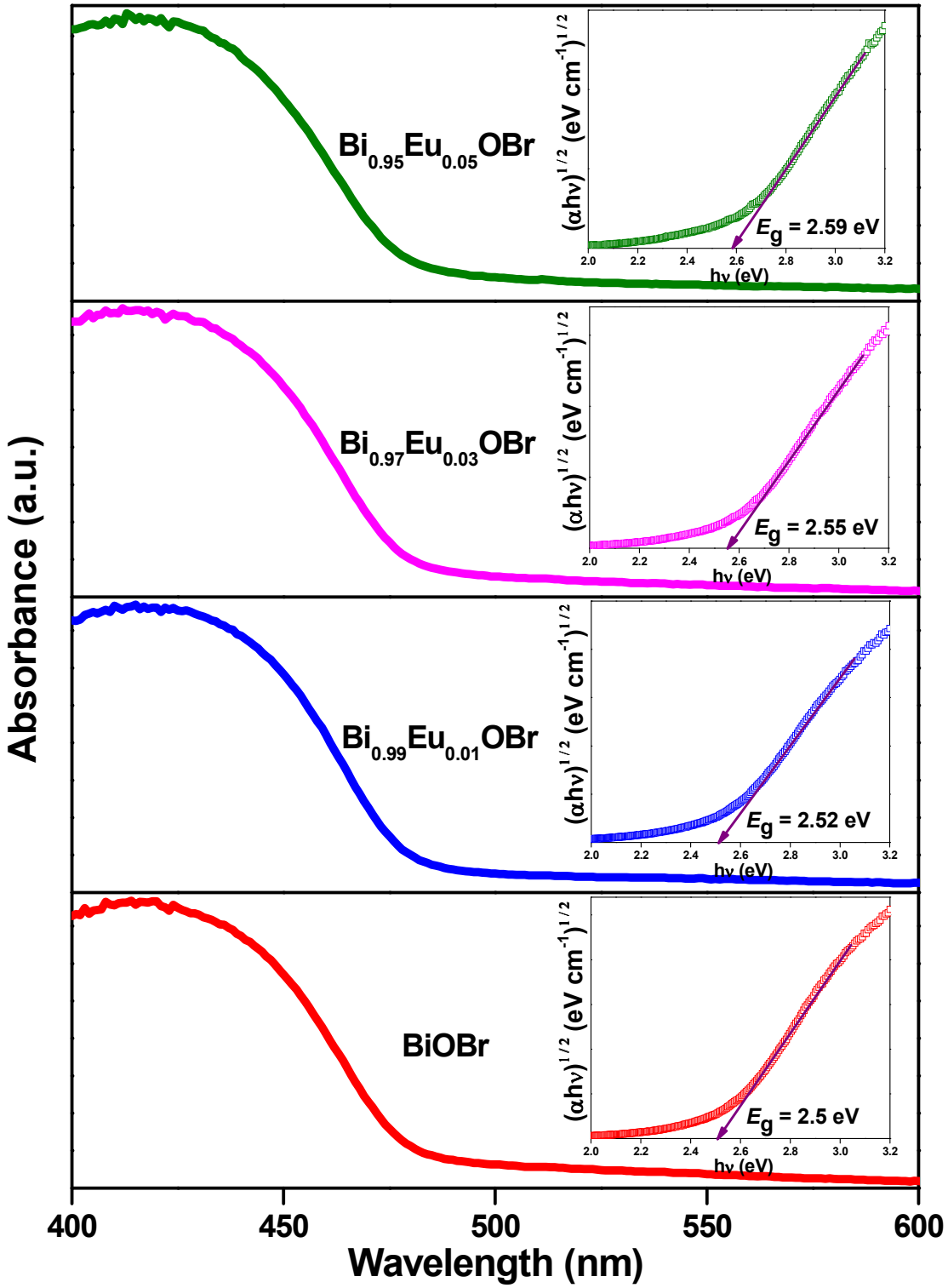

Fig. 5(b)

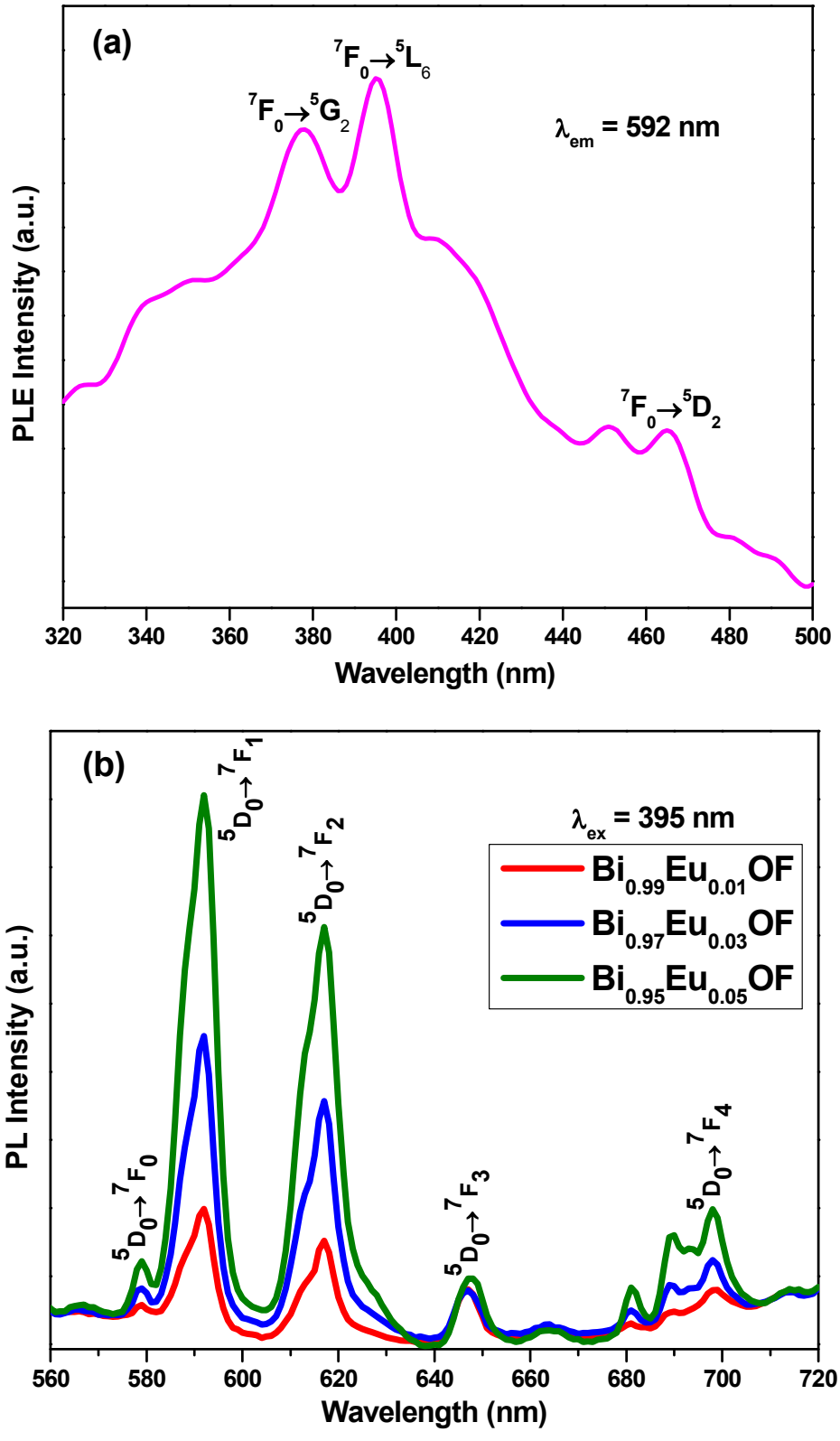

Fig. 6

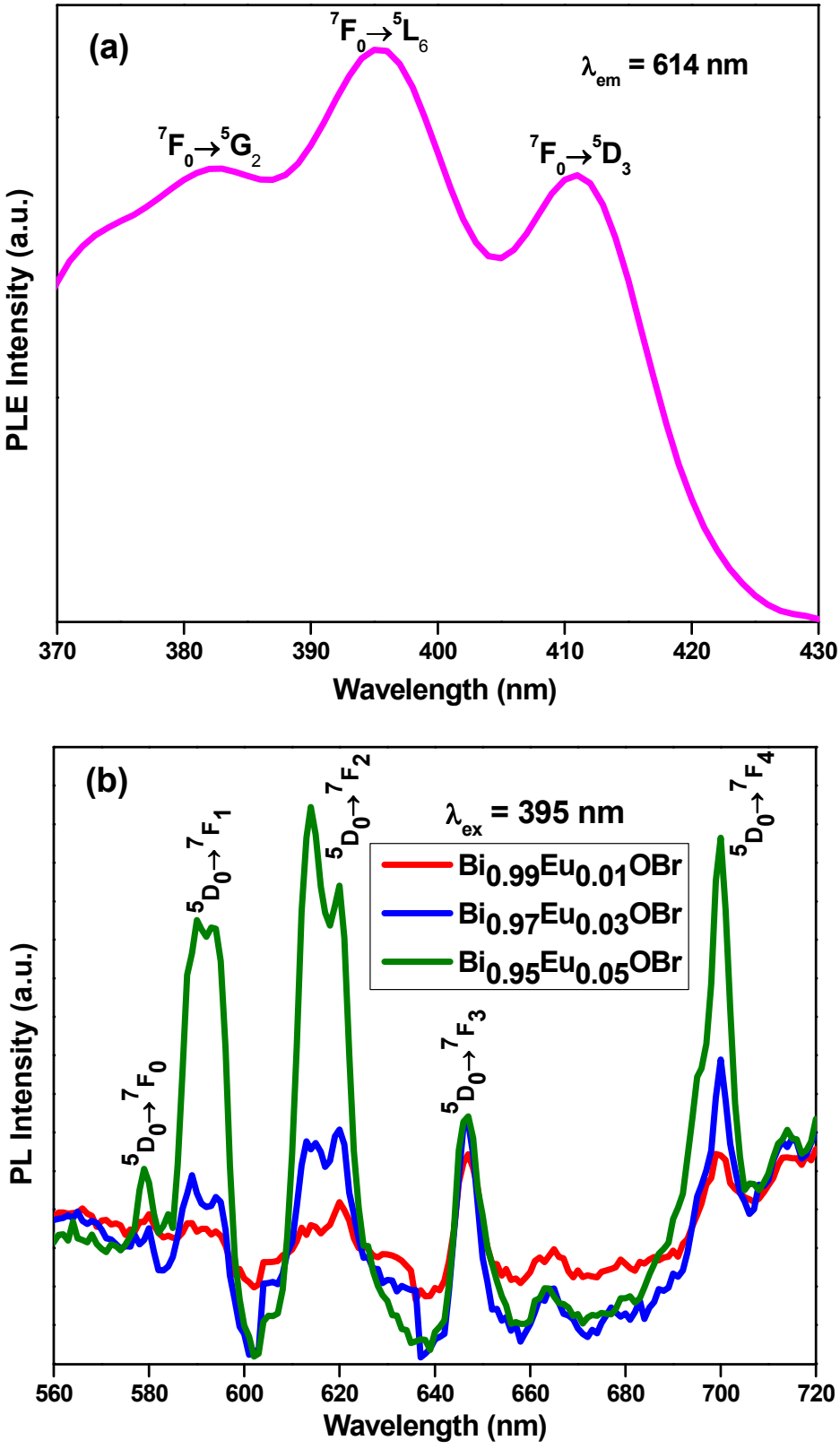

Fig. 7

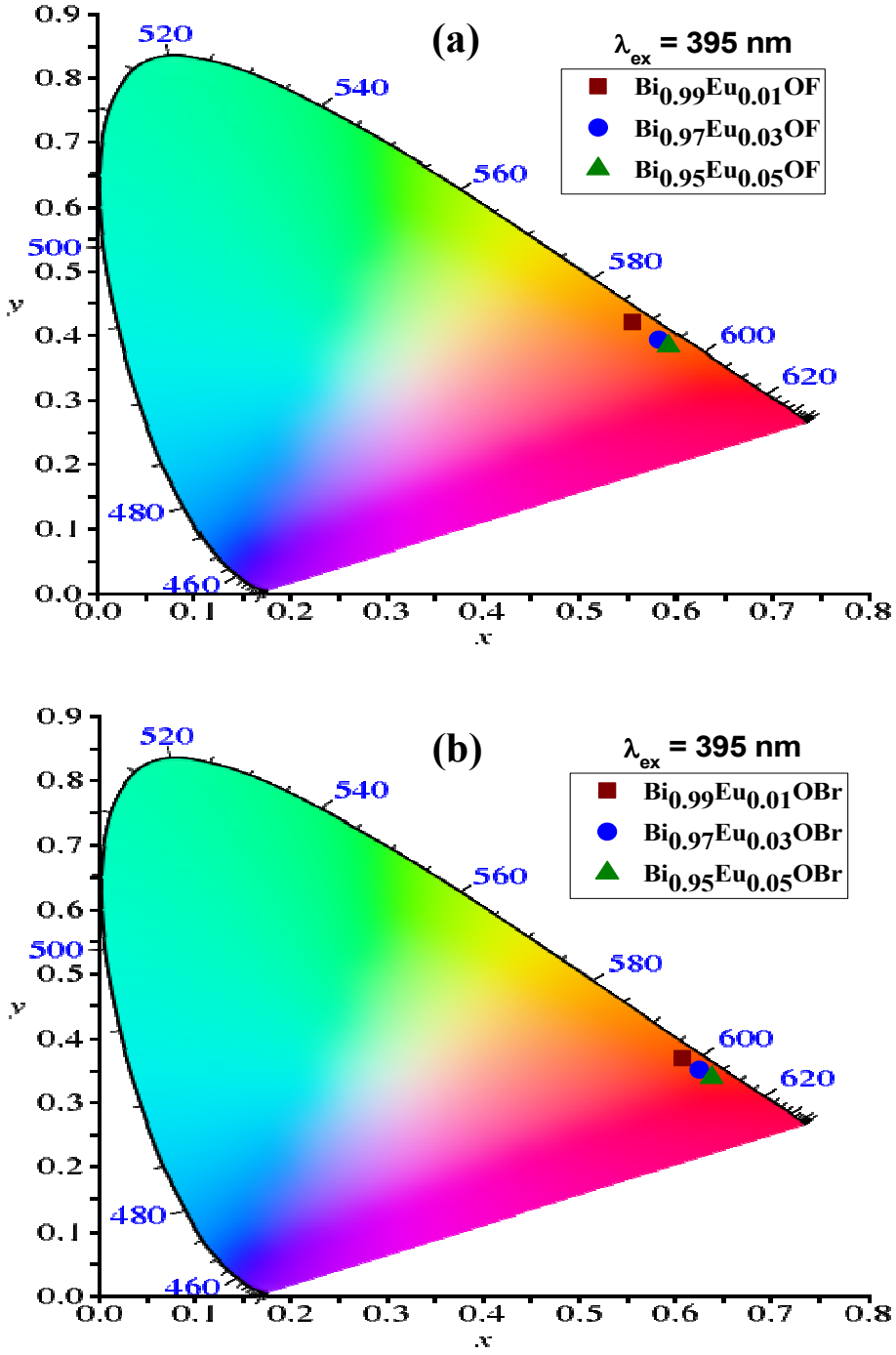

Fig. 8

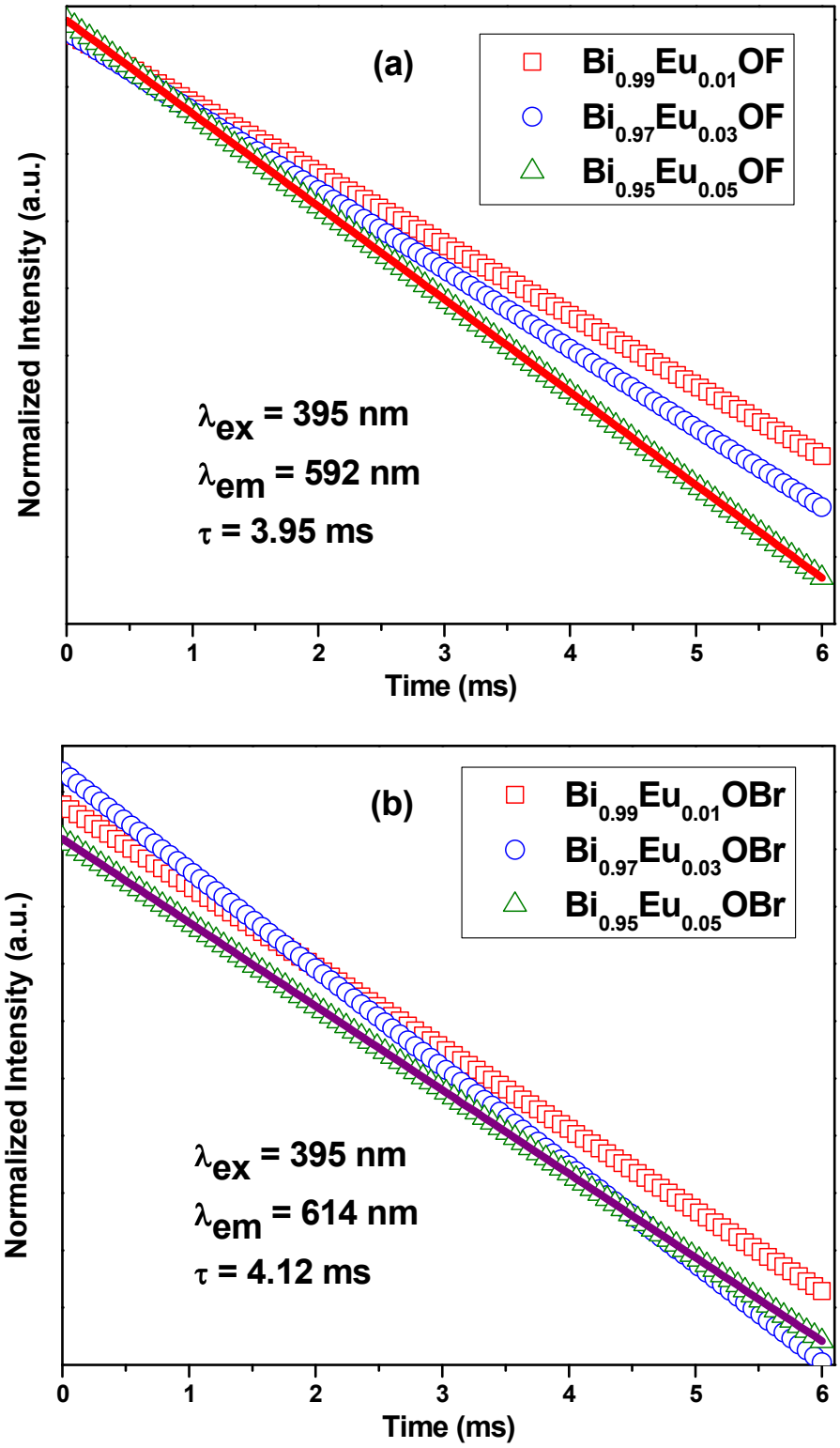

Fig. 9

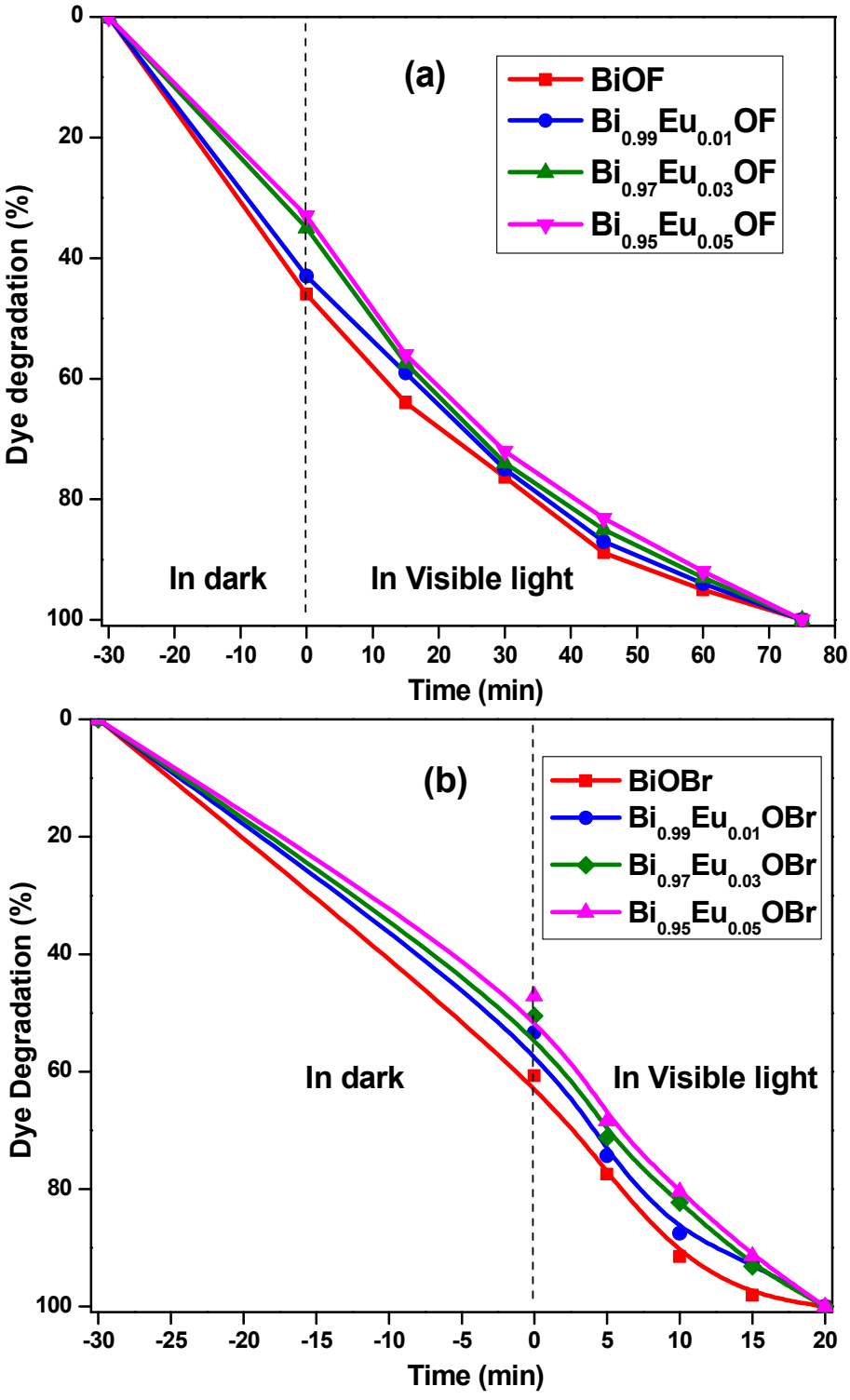

Fig. 10

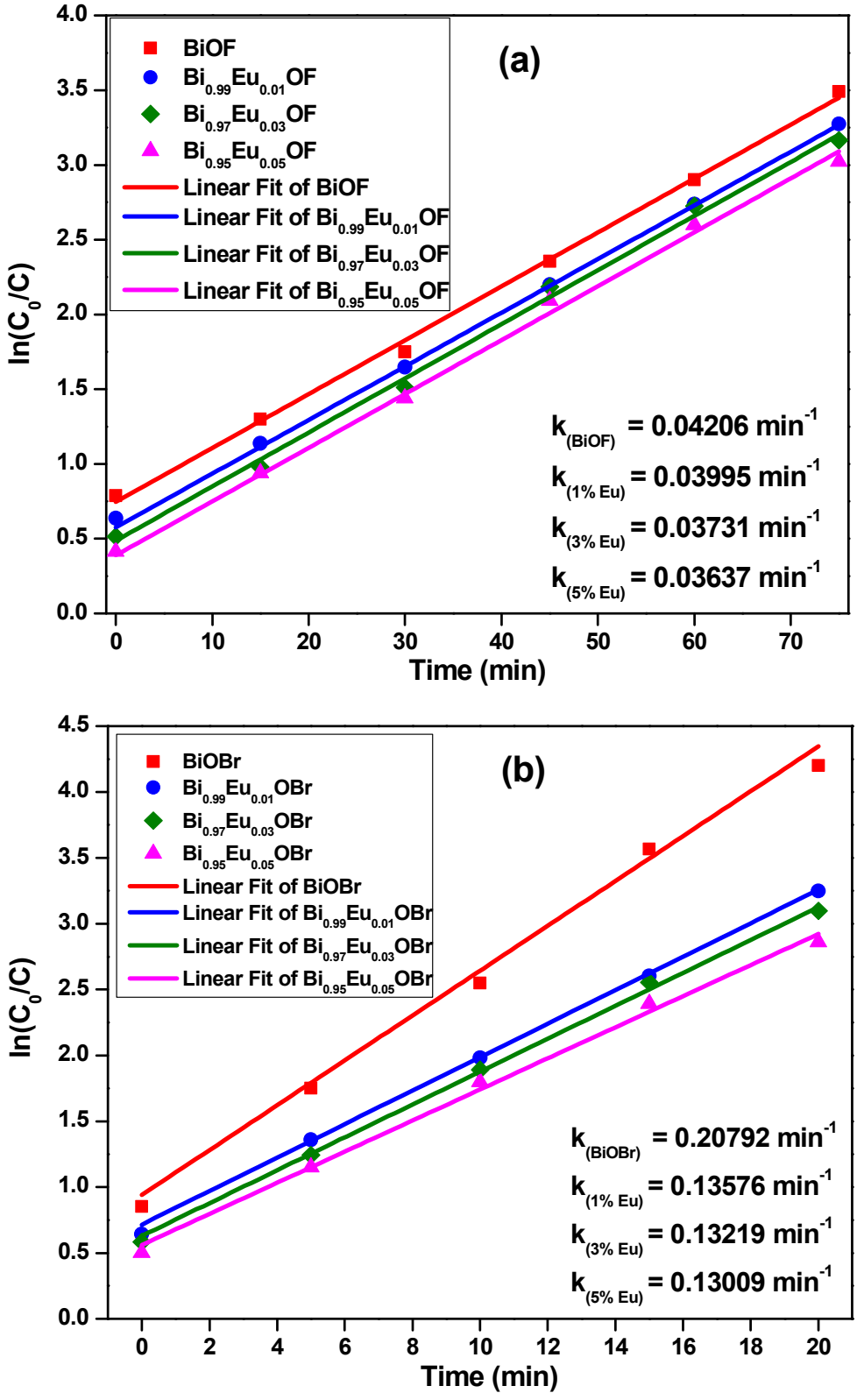

Fig. 11

Graphical Abstract